# Various lithospheric deformation patterns derived from rheological contrasts between continental terranes: Insights from 2-D numerical simulations

Renxian Xie[1, 2], Lin Chen[3], Jason P. Morgan[2], Yongshun John Chen[2*]

[1]School of Transportation Engineering, East China Jiaotong University, Nanchang, 330013, China

[2]Department of Ocean Science and Engineering, Southern University of Science and Technology, Shenzhen, 518055, China

[3]State Key Laboratory of Lithospheric Evolution, Institute of Geology and Geophysics, Chinese Academy of Sciences, Beijing, 100029, China

*Correspondence to*: Yongshun John Chen (johnyc@sustech.edu.cn)

**Abstract.** Continents are formed by the amalgamation of numerous micro-terranes and island arcs, so they have spatially varying lithosphere strengths. The Crème brûlée (CB) model and the Jelly sandwich (JS) model have been commonly used to describe continental lithosphere strength-depth variations. Depending on the strength of continental lower crust, the CB and JS models can be further subdivided into two subclasses, in which the I subclass (CB-I and JS-I) and II subclass (CB-II and JS-II) respectively have a strong or weak lower crust. During continental collision, lithosphere deformation is the byproduct of the comprehensive interaction of multiple terranes. Here we used 2-D thermo-mechanical numerical models that contain three continental terranes to systematically explore the effects of terranes with various strengths on continental deformation, and studied the effects of different rheological assumptions on terrane deformation. We found four types of lithosphere deformation patterns: collision, subduction, thickening and delamination, and replacement. These simulation patterns are seen in observed deformation patterns and structures in East Asia, suggesting they are likely to be naturally occurring modes of intracontinental orogenesis.

## 1. Introduction

Continents have undergone multiple break-up and assembly events during the past ~2 billion years, with the assembly events often being associated with the accretion and deformation of numerous micro-terranes (Mitchell et al., 2021). Accreted terranes have different ages ranging from ~3500 – 3000 Ma to 50 – 0 Ma, and diverse compositions and structures linked to their diverse continental, arc, or

oceanic origin, which often leads to them having distinct initial lithospheric thicknesses and strengths (Artemieva, 2006; Audet and Bürgmann, 2011; Pasyanos et al., 2014; Morgan and Vannucchi, 2022). The lithosphere of ancient continental terranes like cratons are usually thick and strong, while younger lithosphere of continental margins and tectonically active regions is thin and weak (Audet and Bürgmann, 2011; Burov, 2011), and deeply buried former oceanic fragments can have temperature and strengths that vary over ~0.5 Gyr timescale (Morgan and Vannucchi, 2022).

Continental lithosphere strength conventionally been represented by two prevailing rheology models —the Crème brûlée (CB) and the Jelly sandwich (JS) idealizations (Chen and Molnar, 1983; Jackson, 2002; Burov and Watts, 2006; Bürgmann and Dresen, 2008; Burov, 2011). The Crème brûlée scenario suggests that lithosphere strength resides entirely in the crust, with the lithospheric mantle being much weaker (with this strength contrast being the explanation for why little seismicity is typically seen in the continental mantle, despite rock-mechanics arguments that it should usually be stronger than its overlying crust). In contrast, the Jelly sandwich model is based on conventional rock mechanics arguments which imply that in general the continental middle and lower crust should be weaker than overlying cooler upper crust and underlying further-from-solidus lithospheric mantle (Figure 1a). The rheology of the continental lower crust can also differ strongly in different continental terranes due to the varieties in composition, temperature, water content, stress, and tectonic environment (Bürgmann and Dresen, 2008; Hacker et al., 2015; Morgan and Vannucchi, 2022). Therefore, the CB and JS conceptualizations can be further subdivided into CB-I and CB-II, JS-I, and JS-II subclasses that reflect potentially variable strengths of the lower crust: CB-I and JS-I, CB-II and JS-II have strong and weak continental lower crust, respectively (Fig. 1a). Observations in Eastern Asia show a wide variability in terrane deformation styles that argue for the potential feasibility of all four of these rheological models (Figure 1b).

Several previous numerical modelling studies have discussed the effects of rheological contrasts between terranes in lithosphere deformation in a collisional system. Studies containing two terranes have explored contrasts in crustal rheology, and found that this can greatly change the morphology, size and deep lithosphere structure of collisional orogenic belt (Chen, 2021; Chen et al., 2017; Cook and Royden, 2008; Faccenda et al., 2008; Sun and Liu, 2018; Vogt et al., 2018; Xie et al., 2021). Strong crust also has the potential to protect its underlying lithospheric mantle from deformation and destruction (Heron and Pysklywec, 2016). Studies containing three or more terranes in their models

59  have usually focused on the middle terrane which can play a crucial role in lithosphere deformation in a

60  collisional system (Kelly et al., 2016, 2020; Li et al., 2016; Huangfu et al., 2018, 2022; Sun and Liu,

61  2018; Xie et al., 2023). A weak middle terrane is easy to be thickened, to the point where eventually its

62  lithospheric mantle can be delaminated from the crust; while a moderate-strength middle terrane can

63  induce far-field orogenesis; and a strong middle terrane may prevent propagation of deformation and

64  facilitate underthrusting of the advancing terrane. In addition, some studies have also stressed the

65  importance of local pre-existing weak zones which can change the order and style of lithosphere

66  deformation (Chen et al., 2020; Heron et al., 2016; Sokoutis and Willingshofer, 2011; Xie et al., 2021).

67  Large-scale continental collisional system often involves the multiple units of an indenting terrane, a

68  middle terrane, and far-end backwall terranes. These terranes have different lithosphere rheologies and

69  thicknesses, and they collectively contribute to several styles of continental deformation (Artemieva,

70  2006; Audet and Bürgmann, 2011; Pasyanos et al., 2014; Morgan and Vannucchi, 2022). Here, we use a

71  2-D thermo-mechanical numerical modeling method to systematically study the effects of terranes with

72  various rheological properties on continental deformation. Our numerical models simulate a

73  continent-continent collisional system that contains three continental terranes. They explores the effects

74  of four groups of lithosphere deformation patterns linked to the four rheological idealizations of CB-I,

75  CB-II, JS-I, and JS-II applied to each terrane. We will summarize the rheological features for each

76  deformation pattern, and then apply the simulations to better understand ongoing and past deformation

77  histories of various orogenic belts in eastern Asia, such as the eastern Tien Shan orogenic belt, the

78  Tibetan Plateau and the Early Paleozoic Orogen in Southeastern China.

79  **2. Numerical modelling method and model setup**

80  **2.1. Numerical modelling method**

81  Our thermo-mechanical models were performed with the I2VIS code of Gerya and Yuen (2003a),

82  previously used in Xie et al. (2021, 2023). This code combines finite differences with marker-in-cell

83  techniques to solve the mass, momentum, and energy conservation equations for incompressible flow.

84  It incorporates the non-Newtonian visco-plastic rheologies for the lithosphere, as well as the possibility

85  to include parameterizations of the effects of surface processes like sedimentation and erosion.

## 2.1.1. Governing equations

The mass conservation equation for incompressible flow is:

$$\frac{\partial v_x}{\partial x} + \frac{\partial v_y}{\partial y} = 0,\tag{1}$$

The momentum conservation equations (Stokes equations) are:

$$\begin{aligned}\frac{\partial \sigma'_{xx}}{\partial x} + \frac{\partial \sigma'_{xy}}{\partial y} &= \frac{\partial P}{\partial x}\\[6pt]\frac{\partial \sigma'_{yy}}{\partial y} + \frac{\partial \sigma'_{xy}}{\partial x} &= \frac{\partial P}{\partial y} - g\rho\end{aligned},\tag{2}$$

The energy (heat) conservation equation is:

$$\begin{aligned}\rho C_p \frac{DT}{Dt} &= -\frac{\partial q_x}{\partial x} - \frac{\partial q_y}{\partial y} + H_r + H_s + H_a + H_L\\[6pt]q_x &= -k\frac{\partial T}{\partial x}\\[6pt]q_y &= -k\frac{\partial T}{\partial y}\\[6pt]H_a &= T\alpha\frac{DP}{Dt}\\[6pt]H_s &= \sigma'_{xx}\dot{\varepsilon}_{xx} + \sigma'_{yy}\dot{\varepsilon}_{yy} + 2\sigma'_{xy}\dot{\varepsilon}_{xy}\end{aligned},\tag{3}$$

where $x$ and $y$ represent the horizontal and vertical coordinate directions, and $v_x$ and $v_y$ are the corresponding velocity components, respectively. $\sigma'_{ij}$ and $\dot{\varepsilon}_{ij}$ ($i, j = x, y$) are deviatoric stress and strain-rate tensors, respectively; $g$ is the gravitational acceleration; $\rho$ is density. In the heat conservation equation, $q_x$ and $q_y$ are the horizontal and vertical components of the heat flux, respectively; $C_p$ is heat capacity, and $H_r$, $H_a$, $H_s$, and $H_L$ denote the radioactive, adiabatic, shear, and latent heat production, respectively; $k$ is the thermal conductivity.

The rheological constitutive relationship connects the deviatoric stress and strain rate:

$$\begin{aligned}\sigma'_{xx} &= 2\eta_{eff}\dot{\varepsilon}_{xx}, \quad \dot{\varepsilon}_{xx} = \frac{\partial v_x}{\partial x}\\[6pt]\sigma'_{xy} &= 2\eta_{eff}\dot{\varepsilon}_{xy}, \quad \dot{\varepsilon}_{xy} = \frac{1}{2}\left(\frac{\partial v_x}{\partial y} + \frac{\partial v_y}{\partial x}\right),\\[6pt]\sigma'_{yy} &= 2\eta_{eff}\dot{\varepsilon}_{yy}, \quad \dot{\varepsilon}_{yy} = \frac{\partial v_y}{\partial y}\end{aligned}\tag{4}$$

where $\eta_{eff}$ is the effective viscosity.

## 2.1.2. Rheology

Here we make the conventional assumption that the crust and mantle have a visco-plastic rheology. Viscous deformation is determined as a combination of diffusion and dislocation creep that depends on temperature, pressure, and strain rate, expressed as (Gerya, 2019):

$$
\begin{aligned}
\eta_{disl} &= \frac{1}{2} \frac{1}{(A_D)^{-1/n} (\dot{\varepsilon}_{II})^{(n-1)/n}} \exp\left( \frac{E_a + V_a P}{nRT} \right) * S \\
\eta_{diff} &= \frac{1}{2} \frac{A_D}{\sigma_{cr}^{(n-1)}} \exp\left( \frac{E_a + V_a P}{RT} \right) * S
\end{aligned}
\tag{5}
$$

For mineral aggregates, both dislocation and diffusion creep occur simultaneously, with a combined effective viscosity given by:

$$
\frac{1}{\eta_{ductile}} = \frac{1}{\eta_{disl}} + \frac{1}{\eta_{diff}},
\tag{6}
$$

where $\eta_{disl}$ and $\eta_{diff}$ are viscosities for dislocation and diffusion creep, respectively. $\sigma_{cr}$ is the critical stress for the dislocation to diffusion stress transition, and the parameters $A_D$, $E_a$, $V_a$, and $n$ are a material constant, activation energy, activation volume, and stress exponent, respectively, and $R$ is the universal gas constant. The strength scaling factor, $S$, is introduced as a simple parameter to vary the lithospheric viscosity.

Plasticity is implemented using a conventional pseudo-viscous yield criterion first used to study rifting (e.g. Chen and Morgan, 1990) that is extended to include a strain-weakening-like parameterization of fracture-related strain weakening (Gerya et al., 2010; Vogt et al., 2017):

$$\eta_{plastic} = \frac{\sigma_{yield}}{2\dot{\varepsilon}_{II}}$$

$$\sigma_{yield} = C + P\phi$$

118
$$C = \begin{cases} C_a + (C_b - C_a) \times \dfrac{\gamma}{\gamma_{cr}}, & \text{if } \gamma \le \gamma_{cr} \\ C_b, & \text{if } \gamma \ge \gamma_{cr} \end{cases},$$
(7)

$$\phi = \begin{cases} \phi_a + (\phi_b - \phi_a) \times \dfrac{\gamma}{\gamma_{cr}}, & \text{if } \gamma \le \gamma_{cr} \\ \phi_b, & \text{if } \gamma \ge \gamma_{cr} \end{cases}$$

119 where $\sigma_{yield}$ is yield stress, $P$ is dynamic pressure, $\gamma$ is the integrated plastic strain, and $\gamma_{cr}$ is the

120 upper strain limit for fracture-related weakening. $C$ and $\phi$ are cohesion and friction angle that depend

121 on the plastic value. $C_a$ and $\phi_a$ are the initial and $C_b$ and $\phi_b$ are final strength values, respectively.

122 This involves making the rheological assumption that deeply percolating fluids and high pore fluid

123 pressures can significantly lower the plastic strength of fractured rocks.

124 The final effective viscosity is determined by the minimum value between the ductile and plastic

125 viscosities (Ranalli, 1995):

126
$$\eta_{eff} = \min\left(\eta_{ductile}, \eta_{plastic}\right).$$
(8)

127 **2.1.3. Surface processes**

128 Topography in our models evolves according to a transport equation that is solved at each time step,

129 with a crude local parameterization of effects of accounts for sedimentation and erosion:

130
$$\frac{\partial y_{es}}{\partial t} = v_y - v_x \frac{\partial y_{es}}{\partial x} - v_s + v_e.$$
(9)

131 Where $y_{es}$ is the vertical position of the surface as a function of horizontal distance $x$; and $v_x$ and $v_y$ are

132 the corresponding velocity components, respectively. $v_s$ and $v_e$ are the sedimentation and erosion rates,

133 respectively, conforming to the relation:

134 $v_s = 0$ mm/yr, $v_e = 0.3$ mm/yr when $y_{es} > 5$ km;

135 $v_s = 0.3$ mm/yr, $v_e = 0$ mm/yr when $y_{es} < 5$ km.

136 Owing to surface processes are not our focuses in this study, for the aim of simplification, we adopt a

137 small erosion and sedimentation rates of 0.3 mm/yr, which are similar to previous studies (Gerya and

138     Yuan, 2003b; Bian et al., 2020). As well, we simply choose a very large value of 5 km as the threshold

139     for initiating denudation and sedimentation to further weaken the influences of surface processes on the

140     evolutions of our model.

141     **2.2. Model Setup**

142     The 2-D numerical model covers a rectangular computational domain of 3000 km × 700 km and

143     consists of 1360 × 400 non-uniform grid cells with dozens of mobile markers in each grid cell to

144     transport physical properties (Figure 2a). Above 300 km, the cell-size of the grid in the middle of

145     model (X = 1300 – 2200 km) is 1 km × 1 km, and gradually widens towards the two sides to finally

146     become 5 km × 1 km. From the 300 km depth to the model bottom, each grid is stretched to 5 km in the

147     vertical direction. As a result, the grid in the middle of the model (X = 1300 – 2200 km) is 1 km × 5 km

148     and is 5 km × 5 km in the other regions. Changing resolutions in different model regions can ensure the

149     model can finely depict lithosphere deformation in the region of interest while improving the

150     calculation's efficiency.

151     In the initial configuration, the model comprises three continental terranes — the Pro-, Mid- and

152     Retro-terrane — which refer to the indenting 'Pro-' terrane driven by plate convergence, an

153     intermediate 'Mid-' terrane, and a far-end backwall 'Retro-' terrane, respectively (Figure 2a). For the

154     purpose of simplification, the three terranes are assumed to have the same initial crustal structure with

155     20 km thick upper and lower crust, respectively. In the meanwhile, to simulate lateral structure

156     differences within continental lithosphere (Pasyanos et al., 2014), thicknesses of the initial lithospheric

157     mantle of the Pro-, Mid- and Retro-terrane are 160 km, 90 km, and 120 km, respectively. The rest of

158     the region is filled by asthenosphere except along the model top, where a 20 km thick layer of "sticky

159     air" with low viscosity ($1 \times 10^{18}$ Pas) and low density (1 kg/m$^3$) is placed to simulate the effects of a

160     free surface (Schmeling et al., 2008). Flow laws and material properties for each lithospheric layer are

161     listed in Table 1.

162     Mechanical boundary conditions of the model are that the top and sides are free-slip boundaries which

163     mean that the vertical velocity at the top boundary and horizontal velocity at the side boundaries are all

164     zero. The bottom is assumed to be a somewhat non-physical 'permeable boundary' that was developed

165     to reduce the required depth of the computational region (Burg and Gerya, 2005). For top-driven flows

166     like those considered here, this approximation has been shown to not affect deformation in the upper

167   parts of the region (Burg and Gerya, 2005). Finally, a constant convergence rate of 20 mm/yr is

168   assigned to the Pro-terrane (X = 1000 km) to drive the model.

169   Initial temperature conditions are set as follows: the model top is set to 0° C, the two side boundaries

170   are adiabatic boundaries with zero horizontal heat fluxes, and the model bottom has an initial

171   temperature of 1593°C, and can dynamically adjust as the model evolves. The initial thermal gradient

172   in the crust is 15°C/km in the three terranes, so their Moho temperature is 600°C. A temperature of

173   1330°C is applied at the bottom of the lithospheric mantle of the three terranes, which leads to the Pro-

174   and Mid-terrane having minimum and maximal thermal gradients in the lithospheric mantle,

175   respectively (see the right plane in Figure 2a). An adiabatic thermal gradient of 0.5°C/km is assumed

176   within the asthenosphere. The temperature field would evolve over time, thus, although the three

177   terranes are not in thermal equilibrium at the start of the experiments, it has few effects on model

178   evolution. The initial setup of lithosphere structure and temperature field make the Mid-terrane weakest

179   when same rheology model is used for the three terranes.

180   **3. Simulation Results**

181   The rheological models of CB-I, CB-II, JS-I, and JS-II result from different strength scaling factors for

182   the upper crust, the lower crust, and the lithospheric mantle in our numerical models (Figure 2b). We

183   systematically test the effects of these rheological assumptions on the deformation of the Pro-, Mid-

184   and Retro-terranes. According to different behaviors of lithosphere deformation, these simulation

185   results can be categorized into four basic modes of collision, subduction, thickening and delamination,

186   and replacement (Figures S1 and S2). In the deformation mode of collision, the lithospheric mantle of

187   the Mid-terrane is extruded out and the lithospheric mantles of the two bounding terranes meet and

188   collide together. In the deformation mode of subduction, the lithospheric mantle of one of the bounding

189   terranes subducts into the deep mantle below the Mid-terrane while the other one keeps almost

190   undeformed. In the deformation mode of thickening and delamination, one of the bounding terranes is

191   shortened by compression, and delamination may come on the heels of thickening of lithosphere due to

192   gravitational instability in some cases. In the deformation mode of replacement, the bottom of weak

193   and thick lithospheric mantle of the bounding terrane is scraped off by the strong lithospheric mantle of

194   the Mid-terrane, and replaced by the latter. Here, we select a typical case for each mode of lithosphere

195    deformation to describe more details of these modes of model evolution.

### 3.1. Case 1: Lithosphere Collision

197    Case 1 represents the scenario of lithosphere collision (Figure 3). In this model, the assumed

198    rheological models for the Pro-, Mid- and Retro-terrane are JS-I, JS-II, and JS-I, respectively, which

199    means that the Mid-terrane has a significantly weaker lower crust relative to the Pro- and

200    Retro-terranes. The lithospheric mantle of the Mid-terrane is also slightly weaker due to its thinner

201    lithosphere and correspondingly higher initial temperature field. The lithosphere strength profiles of the

202    three terranes are shown in Figure 3g.

203    The Mid-terrane is the first to deform when the Pro-terrane begins to collide, absorbing plate

204    convergence in the form of lithosphere thickening (Figures 3a and 3d). The upper crust of the

205    Mid-terrane breaks due to strain weakening, and several reverse faults are formed to absorb crustal

206    shortening. The lower crust folds, and strain diffusely distributes within it. Since the Retro-terrane is

207    relatively strong, it prevents crustal deformation from propagating into this terrane, and restricts the

208    bulk of deformation to the Mid-terrane. With continuous advance of the Pro-terrane and resistance of

209    the Retro-terrane, the crust of the Mid-terrane is intensively shortened, leading to more thrusting

210    structures in the upper crust and a "flower-like" structure in the lower crust (Figures 3b and 3e). Thrust

211    structures and crustal deformation also expand toward the Pro- and Retro-terranes at this stage.

212    Topography also grows towards the two bounding terranes (Figure 7a). Ultimately, the weak

213    lithospheric mantle of the Mid-terrane is squeezed out, and the Pro- and Retro-terrane's lithospheric

214    mantles meet and so start to collide beneath the overlying crust of the Mid-terrane (Figures 3c and 3f).

### 3.2. Case 2: Lithosphere Subduction

216    Case 2 shows lithosphere subduction of the Pro-terrane (Figure 4). In this model, the assumed

217    rheological models for the Pro-, Mid- and Retro-terrane are JS-II, JS-I, and JS-I, respectively. The

218    Mid-terrane has a stronger lower crust compared with the Pro-terrane, but its lithospheric mantle is a

219    little weaker than the Pro-terrane due to higher temperature field resulting from its thinner lithosphere

220    structure (Figure 4g). When convergence begins, the weak lower crust of the Pro-terrane is blocked by

221    the stronger lower crust of the Mid-terrane. This induces it to stack in a collisional front to form a

222    remarkable folding structure (Figures 4a and 4d). The strong lithospheric mantle of the Pro-terrane

continues to move forward and underthrusts beneath the Mid-terrane. As the Pro-terrane advances, its crust gradually enters the Mid-terrane, inducing shortening and thickening of the upper crust of the Mid-terrane, while the strong lower crust of the Mid-terrane almost keeps undeformed (Figures 4b and 4e).

Meanwhile, the lithospheric mantle of the Pro-terrane continues to underthrust scraping off part of the lithospheric mantle of the Mid-terrane. Eventually, the crust of the Pro-terrane wedges a long distance into the Mid-terrane, and the lithospheric mantle of the Pro-terrane subducts into the deeper mantle (Figures 4d and 4f). In this example, crustal deformation and topography gradually propagate from the Pro-terrane to the Mid-terrane, whereas the Retro-terrane remains nominally 'undeformed' at all times (Figure 7b). In some experiments, the lithospheric mantle of the Retro-terrane can subduct beneath the Mid-terrane (Figure S1).

### 3.3. Case 3: Lithosphere Thickening and Delamination

Case 3 illustrates the thickening and delamination of the lithospheric mantle of the Pro-terrane (Figure 5). In this case, the rheological models for the Pro-, Mid- and Retro-terranes are CB-II, JS-I, and JS-I, respectively (Figure 5j). The Pro-terrane has a rheologically weaker lower crust and lithospheric mantle, making it relatively easy to deform once the collision has started. The lithosphere of the Pro-terrane is first thickened, and the crust starts to fold in two discrete zones (Figures 5a and 5f). The lower part of the thickened lithospheric mantle is denser than its ambient mantle owing to lower temperature, which causes it to drip downwards (Figures 5b–5h). After delamination of the thickened lithosphere, subduction of the Pro-terrane's lithospheric mantle along one of the deformation localization zones absorbs the plate convergence (Figures 5e and 5i). Crustal deformation is restricted in the Pro-terrane until lithosphere delamination, after which crustal strain and topography rapidly spread from the Pro-terrane to the Mid-terrane (Figure 7c). Like case 2, the Retro-terrane stays essentially undeformed at all times.

### 3.4. Case 4: Lithosphere Replacement

Case 4 illustrates how the lithospheric mantle of the Pro-terrane is replaced by that of a neighboring stronger Mid-terrane (Figure 6). In this case, the rheological models for the Pro-, Mid- and Retro-terranes are CB-I, JS-II, and JS-I, respectively. The Pro-terrane has a strong lower crust and a

thick and weak lithospheric mantle, while the Mid-terrane has a weaker lower crust and a strong

lithospheric mantle (Figure 6g). This lithosphere configuration between the Pro- and the Mid-terrane

causes deformation to be primarily distributed in the Pro-terrane's lithospheric mantle and the

Mid-terrane's crust. As a result, the Mid-terrane's crust becomes intensely shortened by fold and thrust

structures, but its strong lithospheric mantle wedges into the Pro-terrane's thick and weak lithospheric

mantle (Figures 6a, 6b, 6d and 6e). The strong lithospheric mantle of the Mid-terrane scrapes off the

lower part of the weak lithospheric mantle of the Pro-terrane and so replaces it (Figures 6c and 6f).

Similar to case 1, crustal deformation and topography expand from the Mid-terrane towards its side

terranes (Figure 7d). The lithospheric mantle of the Retro-terrane can also be replaced in some cases

(e.g. Figure S1).

**4. Discussion**

**4.1. Rheological Characteristics for Distinct Lithosphere Deformation Patterns**

Distinct lithosphere deformation patterns in our simulations arise from rheological contrasts between

neighboring continental terranes. Figure 8 summarizes the rheological characteristics of these distinct

deformation patterns. When the Mid-terrane's lithospheric mantle is weakest (typified by models in

which the rheological model of the Mid-terrane is CB-II), it is easy for its mantle to be extruded out,

leading to collision between the lithospheric mantles of its surrounding Pro- and Retro-terranes. When

one of the two bounding terranes has extremely weak lithospheric mantle, its lithosphere is first to be

thickened by compression, and delamination may follow due to density-driven instability. When the

lower crust of the Mid-terrane is relatively strong (CB-I or JS-I), while the lower crust is weaker in the

Pro- or Retro-terrane (CB-II or JS-II), the lithospheric mantle of the Pro- or Retro-terrane will tend to

subduct into the deep mantle, e.g. leading to intracontinental subduction. Finally, when the Mid-terrane

has a weak lower crust and strong lithospheric mantle (JS-II), while the Pro- or Retro-terrane has a

strong lower crust and weak lithospheric mantle (CB-I), the lithospheric mantle of the former may

replace the lithospheric mantle of the latter.

When the deformation patterns involve the collision and replacement of lithosphere, continental

deformation involves all three terranes (Figures 3 and 6). In contrast, the other deformation patterns

only involve two terranes, the Pro- or Retro-terrane and the Mid-terrane (Figures 4 and 5). The

279    rheological properties of the Mid-terrane are responsible for these differences. Like previous numerical

280    studies (Kelly et al., 2016, 2020; Li et al., 2016; Huangfu et al., 2018, 2022; Sun and Liu, 2018), our

281    simulations show that a weak Mid-terrane is easier to deform, and that in this case lithosphere

282    deformation will expand from center to its neighboring sides; while a relatively strong Mid-terrane

283    prevents deformation from propagating far, so that lithosphere deformation is constrained to occur

284    within two terranes..

285    Although our multi-terrane numerical models mainly focus on the impact of the lateral strength

286    differences between different terranes in a continental collisional system, rheological models of CB-I,

287    CB-II, JS-I, JS-II also involve vertical rheological variation (Figure 1a). It seems difficult to summarize

288    how vertical strength variation affects lithosphere deformation of the continental collisional system.

289    For example, in some cases, only changing the rheological models of the Pro- or Retro-terranes may

290    produce distinct deformation modes such as collision, subduction, thickening and delamination, and

291    displacement (e.g., the first and third rows, the third column in the upper left panel in Figure 8 and the

292    third column in the lower right panel in Figure 8). However, changing the rheological models of the

293    Pro- or Retro-terranes seems to have less impact on the deformation mode of the continental collisional

294    system, according to the simulation results of models which are connected by several cross-shaped

295    solid lines with different colors in Figure 8. Thus, it is difficult to determine whether the horizontal

296    strength contrasts between terranes or the vertical strength variation of a single terrane plays the

297    dominant role in a multi-terrane collisional system. This is also the significance and necessity of our

298    study.

299    **4.2. Influences of Lithosphere Structure**

300    Lithospheric thickness is one of the critical factors that control its strength (Burov, 2011), and it can

301    strongly vary between tectonic regions (Pasyanos et al., 2014). In our models, we assume different

302    lithospheric thicknesses for the Pro-, Mid- and Retro-terrane to explore these effects. Complex effects

303    are seen. When changing the lithospheric thicknesses of the Mid-terrane, or of all three terranes,

304    remarkable variations in lithosphere deformation appear in cases 1 and 2, but smaller variations are

305    seen for cases 3 and 4 (Figure 9). Cases 1 and 2 assume a Jelly sandwich rheology for the Pro-, Mid-

306    and Retro-terrane, so the strength of the lithospheric mantle of three terranes is comparable. Strength

307    variations produced by differences in lithospheric thickness may alter the relative strength of the three

terranes, resulting in distinct lithospheric deformations. For example, if the Pro- and Mid-terranes have same lithosphere thickness, deformation mode in Case 2 would change from subduction to thickening (subplot 3 vs. subplot 8 in Figure 9); if the Mid-terrane is thickest or the three terranes have same thickness of lithosphere, deformation mode in Case 1 would change from collision to replacement (subplot 2 vs. subplot 17 and 22 in Figure 9), and the polarity of the subduction of Pro-terrane's lithospheric mantle would be reversed in Case 2 (subplot 3 vs. subplot 18 and 23 in Figure 9). Instead, in cases 3 and 4, the Pro-, Mid- and Retro-terrane have two regions with stronger Jelly-sandwich-like rheological structures and one with a weaker Crème brûlée structure, and deformation preferentially concentrates in the weaker terrane. In comparison to the large strength difference implied for the lithospheric mantle between the Crème brûlée and Jelly Sandwich rheological models, the strength variations associated with the differences in lithosphere thickness are relatively small. Therefore, changing the thicknesses of the lithosphere has much smaller effects on the lithosphere deformation, as seen in cases 3 and 4 (also see the subplots in 3$^{rd}$ and 4$^{rd}$ rows of Figure 9).

In addition, the weak zones that suture two terranes are generally preserved during continental amalgamation (Burker et al., 1977; Vink et al., 1984; Yin and Harrison, 2000). These local pre-existing lithosphere weaknesses would be preferentially activated if the continental lithosphere were subjected to compression, and could play a key role in concentrating deformation, adjusting deformation sequences, and inducing lithosphere subduction (Sokoutis and Willingshofer, 2011; Heron et al., 2016; Chen et al., 2020; Xie et al., 2021, 2023). Comparing the simulation results of models with and without weak zone, we find that a weak zone will facilitate lithosphere subduction in earlier stages of model evolution, resulting in more diverse lithosphere deformation patterns during the later stage (Figure 10).

**4.3. Implications for the Tectonics of East Asia**

**4.3.1. Lithosphere Collision beneath the Eastern Tien Shan**

The eastern Tien Shan is an ideal region to study the deformation patterns linked to long-term lithosphere collision (Figure 11a). The eastern Tien Shan is bounded by the Tarim Basin to the south, and the Junggar Basin to the north. It is composed of a series of former island arcs and small continental blocks that amalgamated during the late Paleozoic (Han and Zhao, 2017). The lithosphere of the eastern Tien Shan is weaker and thinner in comparison to its neighboring Tarim Basin and Junggar Basin (Kumar et al., 2005; Lei and Zhao et al., 2007; Zhang et al., 2013; Deng and Tesauro,

2016). At ~20 – 25 Ma, the eastern Tien Shan became a reactivated orogeny in response to ongoing India-Asia collision (Yin et al., 1998). Compression linked to the India-Asia collision induced the Tarim lithosphere to underthrust northward (Xu et al., 2002; Guo et al., 2006; Lei and Zhao et al., 2007; Lü et al., 2019; Hapaer et al., 2022; Sun et al., 2022). In the northern part of the eastern Tien Shan, significant high-velocity anomalies and Moho overlap are also imaged, which are conventionally explained as being due to the southward underthrusting of the Junggar lithosphere (Xu et al., 2002; Guo et al., 2006; Li et al., 2016; Lü et al., 2019). High-velocity anomalies in the Tarim and Junggar lithosphere appear to connect beneath the eastern Tien Shan, suggesting the lithosphere of the Tarim and Junggar Basins has converged and collided together in this region (Figure 11b; Lü et al., 2019). Bidirectional underthrusting of the Tarim and Junggar lithosphere leads to intense crustal shortening and thrust faults on both flanks over the adjacent basins, as well as attendant fold and reverse fault zones along the range fronts (Yin et al., 1998; Wang et al., 2004).

**4.3.2. Lithosphere Thickening and Delamination in the Tibetan Plateau**

The deformation pattern arising from lithosphere thickening and delamination has been applied to the Tibetan Plateau (Figure 11c). Tibetan lithosphere may have been significantly weakened by hydration, metasomatism, and partial melting of the lithospheric mantle during a series of oceanic closure and terrane accretion events before the India-Asia collision (Yin and Harrison, 2000; Zhang et al., 2014; Ma et al., 2021). It was then pushed northward by the Indian craton and was blocked by the Tarim/Qaidam craton during India-Asia collision, leading to double crustal thickness (Zhao and Morgan, 1985; Zhang et al., 2011). The lithosphere beneath the Tibetan Plateau does not thicken significantly like its crust, especially beneath northern Tibet (Owens and Zandt, 1997; Tunini et al., 2016). Numerous observations instead suggest that the Tibetan lithosphere has been detached from the crust and has sunk into deeper mantle, consistent with the presence of high-velocity regions in the deep mantle in western, southern and southeastern Tibet (Li et al., 2008; Chen et al., 2017; Feng et al., 2021). A significant depression of the 660-km discontinuity beneath the Himalaya terrane and the uplift of 410-km discontinuity in western Tibet have also attributed to the presence of delaminated Tibetan lithosphere (Wu et al., 2022). In northern Tibet, anomalously high temperatures are assumed to be linked to a region of inefficient $S_n$ propagation indicating a thin or absent lithospheric mantle lid in this region, while a remarkable low-velocity zone in the mantle and ultra-potassic volcanics also suggest

366  lithosphere thinning (Barazangi and Ni, 1982; Turner et al., 1996; Owens and Zandt, 1997; Guo et al.,

367  2006; Liang et al., 2012; Tunini et al., 2016). After lithosphere thinning commenced in the Miocene,

368  the Tibetan Plateau rapidly grew outwards (Lu et al., 2018 and references therein; Molnar et al., 1993;

369  Xie et al., 2023).

370  **4.3.3. Lithosphere Subduction in Southeastern China**

371  An example of intracontinental subduction is the Early Paleozoic Orogen in Southeastern China which

372  appears to have not been preceded by oceanic subduction (Figure 11d; Faure et al., 2009). The

373  northeasterly trending Early Paleozoic Orogen of Southeastern China is located on the Wuyi-Yunkai

374  Fold Belt which welds the Cathaysian Block to the south and the Yangtze Block to the north. Two

375  groups of models of collisional belt (Guo et al., 1989; Hsü et al., 1990) and intercontinental orogen

376  (Faure et al., 2009; Charvet et al., 2010; Li et al., 2010) have been proposed to explain the Early

377  Paleozoic Orogen in Southeastern China. Arguments against it being a collisional orogenic belt are its

378  lack of preserved ophiolites, a magmatic arc, subduction complexes, and high-pressure metamorphism;

379  instead, structural, metamorphic, and sedimentary elements indicate that this orogen was an

380  intracontinental orogen controlled by the northward subduction of Cathaysian Block (Faure et al., 2009;

381  Charvet et al., 2010; Li et al., 2010). At ~465 Ma, the Cathaysian Block underthrust beneath the

382  Yangtze Block along the Jiangshan–Shaoxing Fault, in which the lithospheric weaknesses inherited

383  from previous tectonic event of Nanhua rift at 800 – 850 Ma played an important role (Faure et al.,

384  2009; Charvet et al., 2010). During continental subduction, north-south horizontal shortening is

385  accommodated by ductile decollement zones in the Cathaysian Block, causeing remarkable

386  south-directed crustal folding and thrusting structures related to both thin-skinned and thick-skinned

387  tectonics in the Wuyishan proper and its southern border, and north-directed structures to the west of

388  Ganjiang Fault and north of Jiangshan–Shaoxing Fault, where only thin-skinned tectonics is visible (Li

389  et al., 1998; Shu et al., 1999; Charvet et al., 2010). The tectonic development of the Early Paleozoic

390  Orogen in Southeastern China appears similar to the deformation mode of lithosphere subduction

391  (Figure 4, 10a and 10c).

392  So far, we have yet to find a suitable region to apply the model deformation pattern of lithosphere

393  replacement. In this deformation pattern, crustal deformation and topographic evolution are similar to

394  those in the deformation pattern of lithosphere collision (Figures 7a and 7c). Thus, it is not easy to

395      identify this pattern by geological and geophysical techniques when the replaced and original

396      continental lithosphere has similar properties. Improved imaging observations with better resolution

397      may allow this deformation pattern to be identified in the future.

398      **5. Model Limitations**

399      Although we can obtain four deformation modes of continental lithosphere by changing the rheologies

400      of different terranes in a collisional model, we must keep in mind that our results are based on some

401      simplifications and assumptions, which may affect the model results. For example, in our model three

402      terranes are directly collaged together, but in nature different terranes are often connected through weak

403      sutures which may preferentially deform when they are subjected to compression (Burker et al., 1977;

404      Yin and Harrison, 2000). These local pre-existing weak zones have non-negligible influences on

405      lithospheric deformation, and their role were widely discussed in previous studies (Sokoutis and

406      Willingshofer, 2011; Heron et al., 2016; Chen et al., 2020 ; Xie et al., 2021, 2023). We also discussed

407      the effects of local pre-existing weak zones in Section 4.2. In addition, lithosphere thicknesses of the

408      Pro-, Mid- and Retro-terranes are chosen arbitrary in our models, but they also have important

409      influences on lithosphere deformation (Figure 9). Some studies suggest that differences in crustal

410      strength will also cause different lithospheric deformation (Faccenda et al., 2008; Vogt et al., 2017,

411      2018), but the three terranes are set same crustal structure in our model for the aim of simplification. As

412      well, some studies believe that the convergence rate will greatly affect the deformation of orogenic

413      belts (Chen et al., 2016; Vogt et al., 2017), but in this study, the impact of the convergence rate is not

414      been discussed.

415      **6. Conclusions**

416      The continental lithosphere is likely to have strong lateral variations in its strength. We explored 2-D

417      numerical models that contain three diverse types of continental terranes to study the responses of

418      continental terranes with different strengths to compression. Four rheological models were respectively

419      applied to each of the Pro-, Mid- and Retro-terranes, and simulation results can be grouped into four

420      distinct deformation styles: lithosphere collision, subduction, thickening and delamination, and

421      replacement. These deformation styles arise from the rheological contrasts between the terranes: (1)

when the middle terrane is the weakest, its lithosphere is easily extruded, which leads to lithosphere collision between its two bounding terranes; (2) when the middle terrane has a strong lower crust, while the lower crust of a bounding terrane is weak, then subduction of the lithosphere of the bounding terrane will occur; (3) when a bounding terrane is the weakest, its lithosphere would tend to be thickened by lateral compression, followed by lithosphere delamination due to the resulting density/gravitational instability; (4) when a bounding terrane has a strong lower crust and weak lithospheric mantle, while the middle terrane has a weak lower crust and strong lithospheric mantle, then lithosphere replacement will occur. These simulation patterns are seen in observed deformation patterns and structures in the eastern Tien Shan, and the Tibetan Plateau, the Early Paleozoic Orogen of Southeastern China, suggesting they are likely to be naturally occurring modes of intracontinental orogenesis.

*Code availability*

Requests for the numerical code I2VIS should be sent to the main developer (taras.gerya@erdw.ethz.ch).

*Data availability*

Numerical modeling data and the model evolution animations of Cases 1 – 4 are all provided in Zenodo (https://doi.org/10.5281/zenodo.8354366 and https://doi.org/10.5281/zenodo.10731981).

*Author contribution*: **Conceptualization:** Yongshun John Chen; **Methodology:** Lin Chen, Renxian Xie; **Investigation:** Renxian Xie; **Formal analysis:** Renxian Xie, Lin Chen; **Visualization:** Renxian Xie, Jason P. Morgan; **Writing – original draft preparation:** Renxian Xie; **Funding acquisition:** Yongshun John Chen, Lin Chen, Renxian Xie.

*Competing interests*: The authors declare that they have no conflict of interest.

*Disclaimer. Publisher's note*: Copernicus Publications remains neutral with regard to jurisdictional claims in published maps and institutional affiliations.

## Acknowledgments

The authors sincerely thank Prof. Taras Gerya for providing the I2VIS package and his long-lasting guidance on our geodynamic modeling. We are also grateful to the two anonymous reviewers for their insightful comments, which greatly improved the presentation of the paper. The authors acknowledge that figures of simulation results were prepared with the Generic Mapping Tools (GMT, http://www.soest.hawaii.edu/gmt/), and the color bar of batlow used in the figures of viscosity field is from Crameri et al. (2018). All models were performed on the TianHe-1A system at the National Supercomputer Center in Tianjin.

*Financial support*: This study was supported by the National Natural Science Foundation of China (Grants U1901602), the Shenzhen Science and Technology Programs (KQTD20170810111725321),the National Key R&D Program of China (2022YFF0800800) and National Natural Science Foundation of China (42374076).

## References

Artemieva, I. M.: Global 1× 1 thermal model TC1 for the continental lithosphere: implications for lithosphere secular evolution, Tectonophysics, 416, 245-277, https://doi.org/10.1016/j.tecto.2005.11.022, 2006.

Audet, P., and Bürgmann, R.: Dominant role of tectonic inheritance in supercontinent cycles, Nature

463 geoscience, 4, 184-187, https://doi.org/10.1038/ngeo1080, 2011.

464 Barazangi, M., and Ni, J.: Velocities and propagation characteristics of Pn and Sn beneath the

465 Himalayan arc and Tibetan plateau: Possible evidence for underthrusting of Indian continental

466 lithosphere beneath Tibet, Geology, 10, 179-185,

467 https://doi.org/10.1130/0091-7613(1982)10<179:VAPCOP>2.0.CO;2, 1982.

468 Bian, S., Gong, J., Chen, L., Zuza, A. V., Chen, H., Lin, X., ... & Yang, R.: Diachronous uplift in

469 intra-continental orogeny: 2D thermo-mechanical modeling of the India-Asia collision,

470 Tectonophysics, 775, 228310, https://doi.org/10.1016/j.tecto.2019.228310, 2020.

471 Burg, J. P., and Gerya, T. V.: The role of viscous heating in Barrovian metamorphism of collisional

472 orogens: thermomechanical models and application to the Lepontine Dome in the Central Alps,

473 Journal of Metamorphic Geology, 23, 75-95, https://doi.org/10.1111/j.1525-1314.2005.00563.x,

474 2005.

475 Burke, K., Dewey, J. F., and Kidd, W. S. F.: World distribution of sutures—the sites of former oceans,

476 Tectonophysics, 40, 69-99, https://doi.org/10.1016/0040-1951(77)90030-0, 1977.

477 Burov, E. B., and Watts, A. B.: The long-term strength of continental lithosphere:" jelly sandwich" or"

478 crème brûlée"?. GSA today, 16, 4. , doi: 10.1130/1052-5173(2006)016<4:tltSOc>2.0.cO;2, 1997,

479 2006.

480 Burov, E. B.: Rheology and strength of the lithosphere, Marine and petroleum Geology, 28, 1402-1443,

481 https://doi.org/10.1016/j.marpetgeo.2011.05.008, 2011.

482 Bürgmann, R., and Dresen, G.: Rheology of the lower crust and upper mantle: Evidence from rock

483 mechanics, geodesy, and field observations, Annu. Rev. Earth Planet. Sci., 36, 531-567, doi:

484 10.1146/annurev.earth.36.031207.124326, 2008.

485 Charvet, J., Shu, L., Faure, M., Choulet, F., Wang, B., Lu, H., & Le Breton, N.: Structural development

486 of the Lower Paleozoic belt of South China: genesis of an intracontinental orogeny, Journal of

487 Asian Earth Sciences, 39(4), 309-330, https://doi.org/10.1016/j.jseaes.2010.03.006, 2010.

488 Chen, M., Niu, F., Tromp, J., Lenardic, A., Lee, C. T. A., Cao, W., and Ribeiro, J.: Lithospheric

489 foundering and underthrusting imaged beneath Tibet, Nature communications, 8, 15659,

490 https://doi.org/10.1038/ncomms15659, 2017.

491 Chen, L.: The role of lower crustal rheology in lithospheric delamination during orogeny, Frontiers in

492 Earth Science, 9, 755519, doi: 10.3389/feart.2021.755519, 2021.

Chen, L., Capitanio, F. A., Liu, L., and Gerya, T. V.: Crustal rheology controls on the Tibetan plateau formation during India-Asia convergence, Nature Communications, 8, 15992, https://doi.org/10.1038/ncomms15992, 2017.

Chen, L., & Gerya, T. V.: The role of lateral lithospheric strength heterogeneities in orogenic plateau growth: Insights from 3-D thermo-mechanical modeling, Journal of Geophysical Research: Solid Earth, 121, 3118–3138, https://doi.org/10.1002/2016JB012872.Chen, L., Liu, L., Capitanio, F. A., Gerya, T. V., and Li, Y.: The role of pre-existing weak zones in the formation of the Himalaya and Tibetan plateau: 3-D thermomechanical modelling, Geophysical Journal International, 221, 1971-1983, doi: 10.1093/gji/ggaa125, 2020.

Chen, W. P., and Molnar, P.: Focal depths of intracontinental and intraplate earthquakes and their implications for the thermal and mechanical properties of the lithosphere, Journal of Geophysical Research: Solid Earth, 88, 4183-4214, https://doi.org/10.1029/JB088iB05p04183, 1983.

Chen Y, Morgan W J.: Rift valley/no rift valley transition at mid-ocean ridges, Journal of Geophysical Research: Solid Earth, 95(B11): 17571-17581, https://doi.org/10.1029/JB095iB11p17571, 1990.

Cook, K. L., and Royden, L. H.: The role of crustal strength variations in shaping orogenic plateaus, with application to Tibet, Journal of Geophysical Research: Solid Earth, 113, https://doi.org/10.1029/2007JB005457, 2008.

Crameri, F.: Scientific colour maps, Zenodo,10, 2018, http://doi.org/10.5281/zenodo.1243862.

Deng, Y., and Tesauro, M.: Lithospheric strength variations in Mainland China: Tectonic implications. Tectonics, 35, 2313–2333, https://doi.org/10.1002/2016TC004272, 2016.

Faccenda, M., Gerya, T. V., and Chakraborty, S.: Styles of post-subduction collisional orogeny: Influence of convergence velocity, crustal rheology and radiogenic heat production, Lithos, 103, 257-287, https://doi.org/10.1016/j.lithos.2007.09.009, 2008.

Faure, M., Shu, L., Wang, B., Charvet, J., Choulet, F., and Monie, P.: Intracontinental subduction: a possible mechanism for the Early Palaeozoic Orogen of SE China, Terra Nova, 21, 360-368, https://doi.org/10.1111/j.1365-3121.2009.00888.x, 2009.

Feng, J., Yao, H., Chen, L., and Wang, W.: Massive lithospheric delamination in southeastern Tibet facilitating continental extrusion, National Science Review, 9, nwab174, DOI: 10.1093/nsr/nwab174, 2022.

Gerya, T.: Dynamical instability produces transform faults at mid-ocean ridges, Science, 329,

1047-1050, DOI: 10.1126/science.1191349, 2010.

Gerya, T.: Introduction to numerical geodynamic modelling, 2nd edition, Cambridge University Press, 488pp, ISBN: 9781316534243, https://doi.org/10.1017/9781316534243, 2019.

Gerya, T. V., and Yuen, D. A.: Characteristics-based marker-in-cell method with conservative finite-differences schemes for modeling geological flows with strongly variable transport properties, Physics of the Earth and Planetary Interiors, 140, 293-318, https://doi.org/10.1016/j.pepi.2003.09.006, 2003a.

Gerya, T. V., & Yuen, D. A.: Rayleigh–Taylor instabilities from hydration and melting propel 'cold plumes' at subduction zones, Earth and Planetary Science Letters, 212(1-2), 47-62, https://doi.org/10.1016/S0012-821X(03)00265-6, 2003b.

Guo, B., LIU, Q. Y., CHEN, J. H., ZHAO, D. P., LI, S. C., and LAI, Y. G.: Seismic tomography of the crust and upper mantle structure underneath the Chinese Tianshan, Chinese Journal of Geophysics, 49, 1543-1551, https://doi.org/10.1002/cjg2.982, 2006.

Guo L.Z., Shi Y.S., Lu H.F., Ma R.S., Dong H.G., & Yang S.F.: The pre-Devonian tectonic patterns and evolution of South China, Journal of Southeast Asian Earth Sciences, 3(1-4), 87-93, https://doi.org/10.1016/0743-9547(89)90012-3, 1989.

Hacker, B. R., Kelemen, P. B., and Behn, M. D.: Continental lower crust, Annual Review of Earth and Planetary Sciences, 43, 167-205, doi: 10.1146/annurev-earth-050212-124117, 2015.

Han, Y., and Zhao, G.: Final amalgamation of the Tianshan and Junggar orogenic collage in the southwestern Central Asian Orogenic Belt: Constraints on the closure of the Paleo-Asian Ocean, Earth-Science Reviews, 186, 129-152, https://doi.org/10.1016/j.earscirev.2017.09.012, 2018.

Hapaer, T., Tang, Q., Sun, W., Ao, S., Zhao, L., Hu, J., ... and Xiao, W.: Opposite facing dipping structure in the uppermost mantle beneath the central Tien Shan from Pn traveltime tomography, International Journal of Earth Sciences, 111, 2571-2584, https://doi.org/10.1007/s00531-022-02162-9, 2022.

Heron, P. J., and Pysklywec, R. N.: Inherited structure and coupled crust-mantle lithosphere evolution: Numerical models of Central Australia, Geophysical Research Letters, 43, 4962-4970, https://doi.org/10.1002/2016GL068562, 2016.

Heron, P. J., Pysklywec, R. N., and Stephenson, R.: Lasting mantle scars lead to perennial plate tectonics, Nature communications, 7, 11834, https://doi.org/10.1038/ncomms11834, 2016.

553 Hsü, K. J., Li, J., Chen, H., Wang, Q., Sun, S., & Şengör, A. M. C.: Tectonics of South China: key to

554 understanding West Pacific geology, Tectonophysics, 183(1-4), 9-39,

555 https://doi.org/10.1016/0040-1951(90)90186-C, 1990.

556 Huangfu, P., Li, Z. H., Gerya, T., Fan, W., Zhang, K. J., Zhang, H., and Shi, Y.: Multi-terrane structure

557 controls the contrasting lithospheric evolution beneath the western and central–eastern Tibetan

558 plateau, Nature Communications, 9, 3780, https://doi.org/10.1038/s41467-018-06233-x, 2018.

559 Huangfu, P., Li, Z. H., Fan, W., Zhang, K. J., and Shi, Y.: Contrasting collision-induced far-field

560 orogenesis controlled by thermo-rheological properties of the composite terrane, Gondwana

561 Research, 103, 404-423, https://doi.org/10.1016/j.gr.2021.10.020, 2022.

562 Jackson, J. A.: Strength of the continental lithosphere: time to abandon the jelly sandwich?, GSA today,

563 12, 4-10, DOI: 10.1130/1052-5173(2002)012<0004:SOTCLT>2.0.CO;2, 2002.

564 Junmeng, Z., Guodong, L., Zaoxun, L., Xiankang, Z., and Guoze, Z.: Lithospheric structure and

565 dynamic processes of the Tianshan orogenic belt and the Junggar basin, Tectonophysics, 376,

566 199-239, https://doi.org/10.1016/j.tecto.2003.07.001, 2003.

567 Kelly, S., Butler, J. P., and Beaumont, C.: Continental collision with a sandwiched accreted terrane:

568 Insights into Himalayan–Tibetan lithospheric mantle tectonics?, Earth and Planetary Science

569 Letters, 455, 176-195, https://doi.org/10.1016/j.epsl.2016.08.039, 2016.

570 Kelly, S., Beaumont, C., and Butler, J. P.: Inherited terrane properties explain enigmatic post-collisional

571 Himalayan-Tibetan evolution, Geology, 48, 8-14, https://doi.org/10.1130/G46701.1, 2020.

572 Kumar, P., Yuan, X., Kind, R., and Kosarev, G.: The lithosphere-asthenosphere boundary in the Tien

573 Shan-Karakoram region from S receiver functions: Evidence for continental subduction,

574 Geophysical Research Letters, 32, https://doi.org/10.1029/2004GL022291, 2005.

575 Lei, J., and Zhao, D.: Teleseismic P-wave tomography and the upper mantle structure of the central

576 Tien Shan orogenic belt, Physics of the Earth and Planetary Interiors, 162, 165-185,

577 https://doi.org/10.1016/j.pepi.2007.04.010, 2007.

578 Li, C., Van der Hilst, R. D., Meltzer, A. S., and Engdahl, E. R.: Subduction of the Indian lithosphere

579 beneath the Tibetan Plateau and Burma, Earth and Planetary Science Letters, 274, 157-168,

580 https://doi.org/10.1016/j.epsl.2008.07.016, 2008.

581 Li, J., Zhang, J., Zhao, X., Jiang, M., Li, Y., Zhu, Z., ... and Yang, T.: Mantle subduction and uplift of

582 intracontinental mountains: A case study from the Chinese Tianshan Mountains within Eurasia,

Scientific Reports, 6, 28831, https://doi.org/10.1038/srep28831, 2016.

Li, Z. H., Liu, M., and Gerya, T.: Lithosphere delamination in continental collisional orogens: A systematic numerical study, Journal of Geophysical Research: Solid Earth, 121, 5186-5211, https://doi.org/10.1002/2016JB013106, 2016.

Li, Z. X.: Tectonic history of the major east Asian lithospheric blocks since the mid‐Proterozoic—a synthesis, Mantle dynamics and plate interactions in East Asia, 27, 221-243, https://doi.org/10.1029/GD027p0221, 1998.

Li, Z. X., Li, X. H., Wartho, J. A., Clark, C., Li, W. X., Zhang, C. L., & Bao, C..: Magmatic and metamorphic events during the early Paleozoic Wuyi-Yunkai orogeny, southeastern South China: New age constraints and pressure-temperature conditions, GSA Bulletin, 122(5-6), 772-793, https://doi.org/10.1130/B30021.1, 2010.

Liang, X., Sandvol, E., Chen, Y. J., Hearn, T., Ni, J., Klemperer, S., ... & Tilmann, F.: A complex Tibetan upper mantle: A fragmented Indian slab and no south-verging subduction of Eurasian lithosphere, Earth and Planetary Science Letters, 333, 101-111, https://doi.org/10.1016/j.epsl.2012.03.036, 2012.

Lu, H., Tian, X., Yun, K., and Li, H.: Convective removal of the Tibetan Plateau mantle lithosphere by~ 26 Ma, Tectonophysics, 731, 17-34, https://doi.org/10.1016/j.tecto.2018.03.006, 2018.

Lü, Z., Gao, H., Lei, J., Yang, X., Rathnayaka, S., and Li, C.: Crustal and upper mantle structure of the Tien Shan orogenic belt from full-wave ambient noise tomography, Journal of Geophysical Research: Solid Earth, 124, 3987-4000, https://doi.org/10.1029/2019JB017387, 2019.

Ma, L., Wang, Q., Kerr, A. C., and Tang, G. J.: Nature of the pre-collisional lithospheric mantle in central Tibet: Insights to Tibetan Plateau uplift, Lithos, 388, 106076, https://doi.org/10.1016/j.lithos.2021.106076, 2021.

Mitchell, R. N., Zhang, N., Salminen, J., Liu, Y., Spencer, C. J., Steinberger, B., ... and Li, Z. X. : The supercontinent cycle, Nature Reviews Earth and Environment, 2, 358-374, https://doi.org/10.1038/s43017-021-00160-0, 2021.

Molnar, P., England, P., and Martinod, J.: Mantle dynamics, uplift of the Tibetan Plateau, and the Indian monsoon, Reviews of Geophysics, 31, 357-396, https://doi.org/10.1029/93RG02030, 1993.

Morgan J P, Vannucchi P. : Transmogrification of ocean into continent: implications for continental evolution, Proceedings of the National Academy of Sciences, 119(15): e2122694119,

https://doi.org/10.1073/pnas.2122694119, 2022.Owens, T. J., and Zandt, G.: Implications of crustal property variations for models of Tibetan plateau evolution, Nature, 387, 37-43, https://doi.org/10.1038/387037a0, 1997.

Pasyanos, M. E., Masters, T. G., Laske, G., and Ma, Z.: LITHO1. 0: An updated crust and lithospheric model of the Earth, Journal of Geophysical Research: Solid Earth, 119, 2153-2173, https://doi.org/10.1002/2013JB010626, 2014.

Ranalli, G.: Rheology of the Earth, 2$^{nd}$ Edition, Springer Science and Business Media, 421pp, ISBN 0412546701, 1995.

Schmeling, H., Babeyko, A. Y., Enns, A., Faccenna, C., Funiciello, F., Gerya, T., ... and Van Hunen, J.: A benchmark comparison of spontaneous subduction models—Towards a free surface, Physics of the Earth and Planetary Interiors, 171, 198-223, https://doi.org/10.1016/j.pepi.2008.06.028, 2008.

Shu L.S., Lu H.F., Jia D.: Study of the $^{40}$Ar/$^{39}$Ar Isotopic Age for the Early Paleozoic Tectonothermal Event in the Wuyishan Region, South China, Journal-Nanjing University Natural Sciences Edition, 35(6), 668-674, 1999.

Sokoutis, D., and Willingshofer, E.: Decoupling during continental collision and intra-plate deformation, Earth and Planetary Science Letters, 305, 435-444, https://doi.org/10.1016/j.epsl.2011.03.028, 2011.

Sun, W., Ao, S., Tang, Q., Malusà, M. G., Zhao, L., and Xiao, W.: Forced Cenozoic continental subduction of Tarim craton-like lithosphere below the Tianshan revealed by ambient noise tomography, Geology, 50, 1393-1397, https://doi.org/10.1130/G50510.1, 2022.

Sun, Y., and Liu, M.: Rheological control of lateral growth of the Tibetan Plateau: Numerical results, Journal of Geophysical Research: Solid Earth, 123, 10-124, https://doi.org/10.1029/2018JB016601, 2018.

Tunini, L., Jimenez-Munt, I., Fernandez, M., Verges, J., Villasenor, A., Melchiorre, M., and Afonso, J. C.: Geophysical-petrological model of the crust and upper mantle in the India-Eurasia collision zone, Tectonics, 35, 1642–1669, https://doi.org/10.1002/2016TC004161, 2016.

Turner, S., Arnaud, N., Liu, J., Rogers, N., Hawkesworth, C., Harris, N., ... and Deng, W.: Post-collision, shoshonitic volcanism on the Tibetan Plateau: implications for convective thinning of the lithosphere and the source of ocean island basalts, Journal of petrology, 37, 45-71, https://doi.org/10.1093/petrology/37.1.45, 1996.

Vink G E, Morgan W J, Zhao W L: Preferential rifting of continents: a source of displaced terranes[J]. Journal of Geophysical Research: Solid Earth, 89(B12): 10072-10076, https://doi.org/10.1029/JB089iB12p10072, 1984.

Vogt, K., Matenco, L., and Cloetingh, S.: Crustal mechanics control the geometry of mountain belts. Insights from numerical modelling, Earth and Planetary Science Letters, 460, 12-21, https://doi.org/10.1016/j.epsl.2016.11.016, 2017.

Vogt, K., Willingshofer, E., Matenco, L., Sokoutis, D., Gerya, T., and Cloetingh, S.: The role of lateral strength contrasts in orogenesis: A 2D numerical study, Tectonophysics, 746, 549-561, https://doi.org/10.1016/j.tecto.2017.08.010, 2018.

Wang, C. Y., Yang, Z. E., Luo, H., and Mooney, W. D.: Crustal structure of the northern margin of the eastern Tien Shan, China, and its tectonic implications for the 1906 M~7.7 Manas earthquake, Earth and Planetary Science Letters, 223, 187-202, https://doi.org/10.1016/j.epsl.2004.04.015, 2004.

Wang, M., and Shen, Z. K.: Present-day crustal deformation of continental China derived from GPS and its tectonic implications, Journal of Geophysical Research: Solid Earth, 125, e2019JB018774, https://doi.org/10.1029/2019JB018774, 2020.

Wu, Y., Bao, X., Zhang, B., Xu, Y., and Yang, W.: Seismic evidence for stepwise lithospheric delamination beneath the Tibetan Plateau, Geophysical Research Letters, 49, e2022GL098528, https://doi.org/10.1029/2022GL098528, 2022.

Xie, R., Chen, L., Xiong, X., Wang, K., and Yan, Z.: The Role of Pre-existing Crustal Weaknesses in the Uplift of the Eastern Tibetan Plateau: 2D Thermo-Mechanical Modeling, Tectonics, 40, e2020TC006444, https://doi.org/10.1029/2020TC006444, 2021.

Xie, R., Chen, L., Yin, A., Xiong, X., Chen, Y. J., Guo, Z., and Wang, K.: Two phases of crustal shortening in northeastern Tibet as a result of a stronger Qaidam lithosphere during the Cenozoic India–Asia collision, Tectonics, 42, e2022TC007261, https://doi.org/10.1029/2022TC007261, 2023.

Xu, Y., Liu, F., Liu, J., and Chen, H.: Crust and upper mantle structure beneath western China from P wave travel time tomography, Journal of Geophysical Research: Solid Earth, 107, ESE-4, https://doi.org/10.1029/2001JB000402, 2002.

Yin, A., Nie, S., Craig, P., Harrison, T. M., Ryerson, F. J., Xianglin, Q., and Geng, Y.: Late Cenozoic

673      tectonic evolution of the southern Chinese Tian Shan, Tectonics, 17, 1-27,
674      https://doi.org/10.1029/97TC03140, 1998.

675    Yin, A., and Harrison, T. M.: Geologic evolution of the Himalayan-Tibetan orogen, Annual review of
676      earth and planetary sciences, 28, 211-280, https://doi.org/10.1146/annurev.earth.28.1.211, 2000.

677    Zhang, Z., Deng, Y., Teng, J., Wang, C., Gao, R., Chen, Y., and Fan, W.: An overview of the crustal
678      structure of the Tibetan plateau after 35 years of deep seismic soundings, Journal of Asian Earth
679      Sciences, 40, 977-989, https://doi.org/10.1016/j.jseaes.2010.03.010, 2011.

680    Zhang, Z., Deng, Y., Chen, L., Wu, J., Teng, J., and Panza, G.: Seismic structure and rheology of the
681      crust under mainland China, Gondwana Research, 23, 1455-1483,
682      https://doi.org/10.1016/j.gr.2012.07.010, 2013.

683    Zhang, Z., Teng, J., Romanelli, F., Braitenberg, C., Ding, Z., Zhang, X., ... & Panza, G. F.: Geophysical
684      constraints on the link between cratonization and orogeny: Evidence from the Tibetan Plateau and
685      the North China Craton. Earth-Science Reviews, 130, 1-48,
686      https://doi.org/10.1016/j.earscirev.2013.12.005, 2014.

687    Zhao W L, Morgan W J.: Uplift of Tibetan plateau, Tectonics, 4(4),
688      359-369, https://doi.org/10.1029/TC004i004p00359, 1985.

689

690

 **Figures and captions**

692
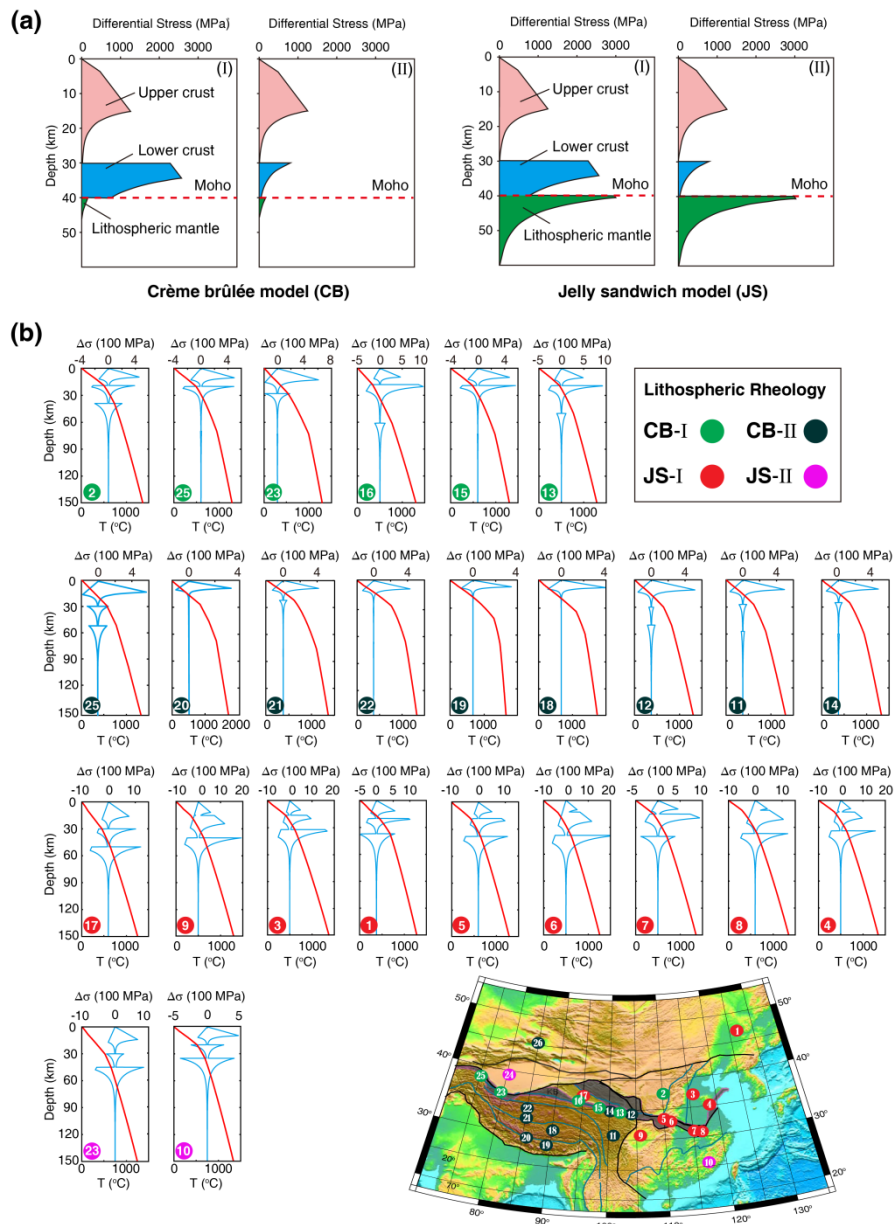
**Figure 1. Four rheological models of continental lithosphere.** (a) Crème brûlée model (CB) and Jelly sandwich model (JS). The two rheological models can be further subdivided into CB-I, CB-II, JS-I, and JS-II according to the strength of the lower crust (modified from Jackson, 2002). (b) Observations of four distinct lithosphere rheological structures implied for East Asia (modified from Zhang et al., 2013). Locations of strength profiles are pointed out by dots with numbers in the topography map. Dots filled with different colors indicate different models of lithospheric rheology. These strength profiles are calculated based on observed geothermal structure and lithospheric structure, and assumed that compositions of the upper and lower crust and lithospheric mantle are wet quartzite, undried granulite and dry olivine, respectively. Variations of temperature and lithospheric compositions

701 lead to a diverse suite of strength profiles vs. depth.

702
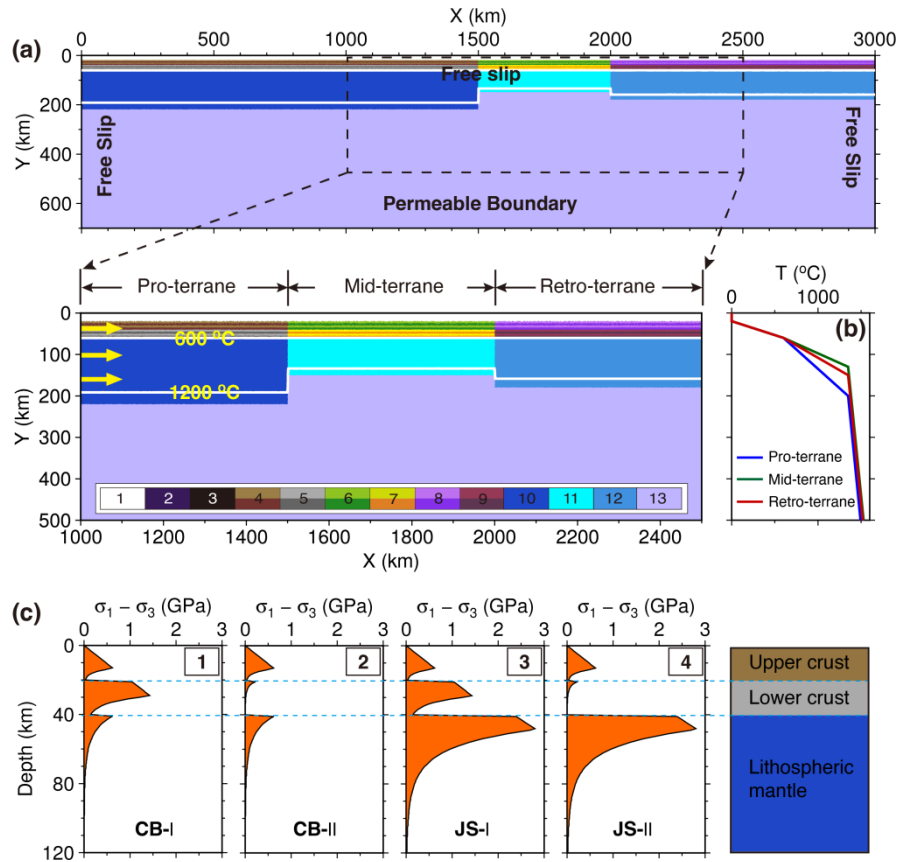
703
704 **Figure 2. Initial model setup.** (a) Initial model configuration. The model size is 3000 km × 700 km, and size of

705 study region is 1500 km × 500 km. Three continental terranes of the Pro-, Mid- and Retro-terranes are contained

706 in the numerical model, and they are 200 km, 130 km, and 160 km thick, respectively. White lines are isotherms

707 with an interval of 600°C. Yellow arrows indicate the convergence rate of 20 mm/yr. Colored grids: 1 – sticky air;

708 2 – sediments; 3 – weak zone; 4, 6, 8 – the upper crust of the Pro-, Mid- and Retro-terranes, respectively; 5, 7, 9 –

709 the lower crust of the Pro-, Mid- and Retro-terranes, respectively; 10, 11, 12 –lithospheric mantle of the Pro-,

710 Mid- and Retro-terranes, respectively; 13 – asthenosphere. (b) Initial temperature structure for the three terranes.

711 The Pro- and Mid-terranes respectively have a coldest and warmest lithospheric mantle due to their differences of

712 lithosphere thicknesses. (c) Four rheological models with contrasting lithospheric strength profiles. These are

713 derived from different strength scaling factor ($S$) combinations for the upper crust, lower crust, and lithospheric

714 mantle (Table S1). Strength profiles are calculated based on the Pro-terrane's initial lithospheric structure,

715 composition, and temperature field. The prescribed strain rate is $1 \times 10^{-14}$ s$^{-1}$. CB-I and CB-II, the crème brûlée

716 model with strong and weak lower crust, respectively; JS-I and JS-II, the jelly sandwich model with strong and

717 weak lower crust, respectively.

718

719
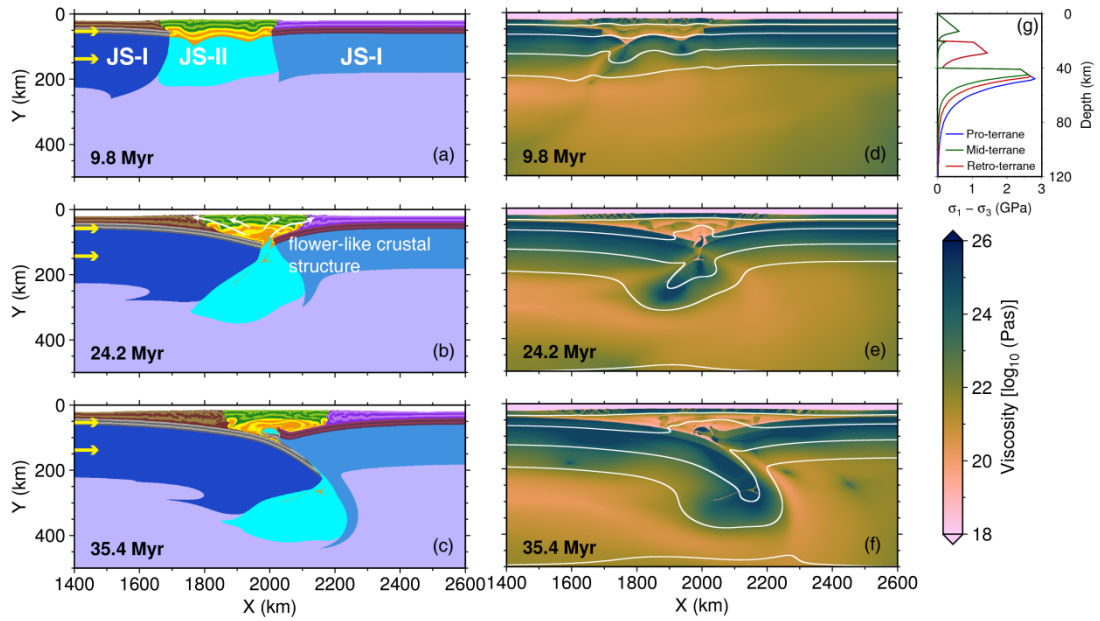
**Figure 3. Collision of the lithospheres of the Pro- and Retro-terranes.** Rheological models for the Pro-, Mid-and Retro-terranes are JS-I, JS-II, and JS-I, respectively, as shown in (g). The left panel shows compositional fields at 9.8 Myr, 24.2 Myr, and 35.4 Myr, respectively. Yellow arrows indicate the convergence rate. The right panel shows the corresponding viscosities. White lines are isotherms with an interval of 300° C.

724

725
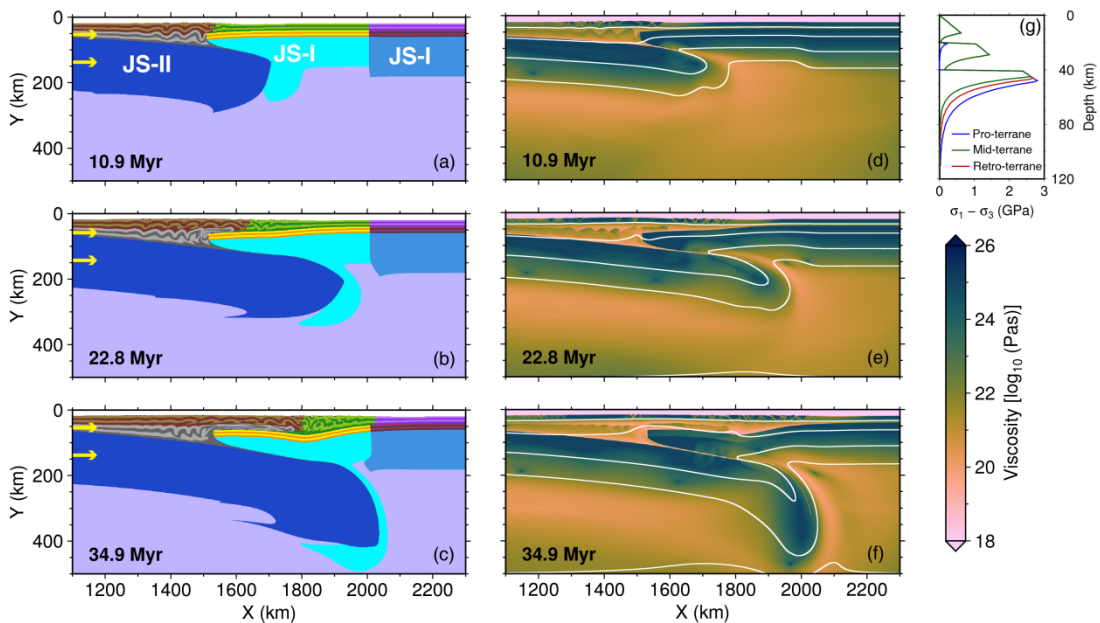
**Figure 4. Subduction of the lithosphere of the Pro-terrane.** Rheological models for the Pro-, Mid- and Retro-terranes are JS-II, JS-I, and JS-I, respectively. See Figure 3 for plotting conventions.

728

729
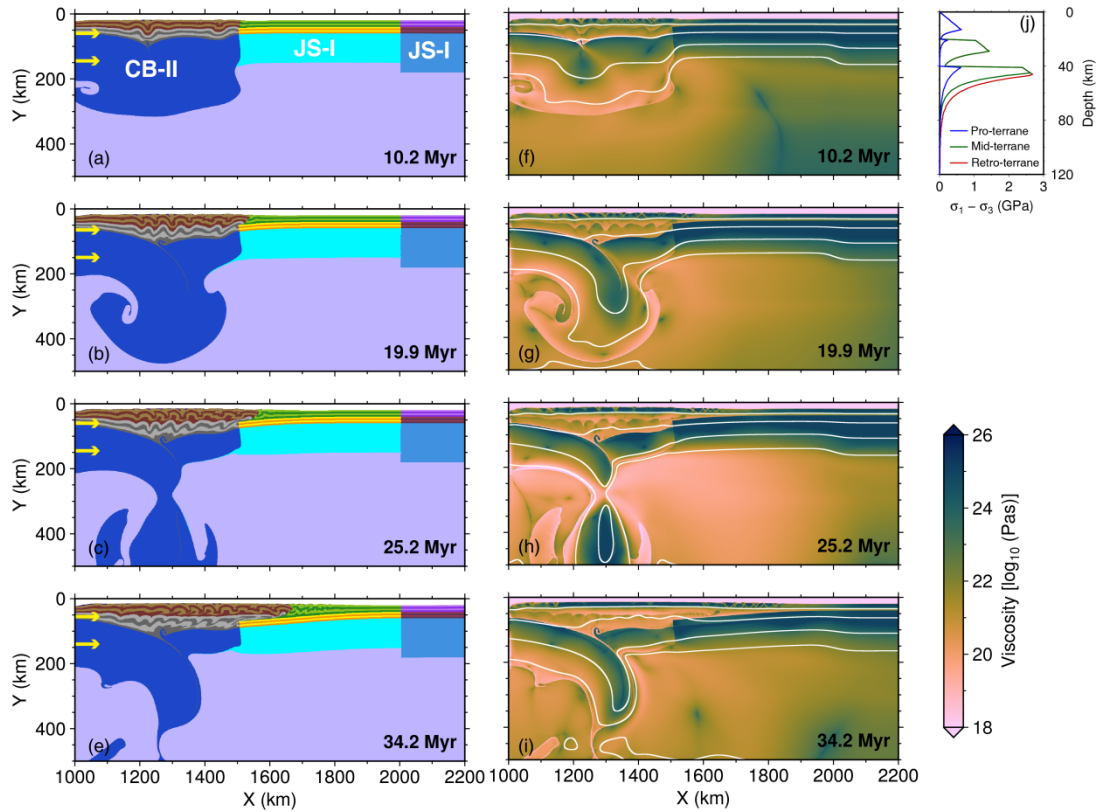
**Figure 5. Thickening and delamination of the lithosphere of the Pro-terrane.** Rheological models for the Pro-,

Mid- and Retro-terranes are CB-II, JS-I, and JS-I, respectively. See Figure 3 for plotting conventions.

732

733
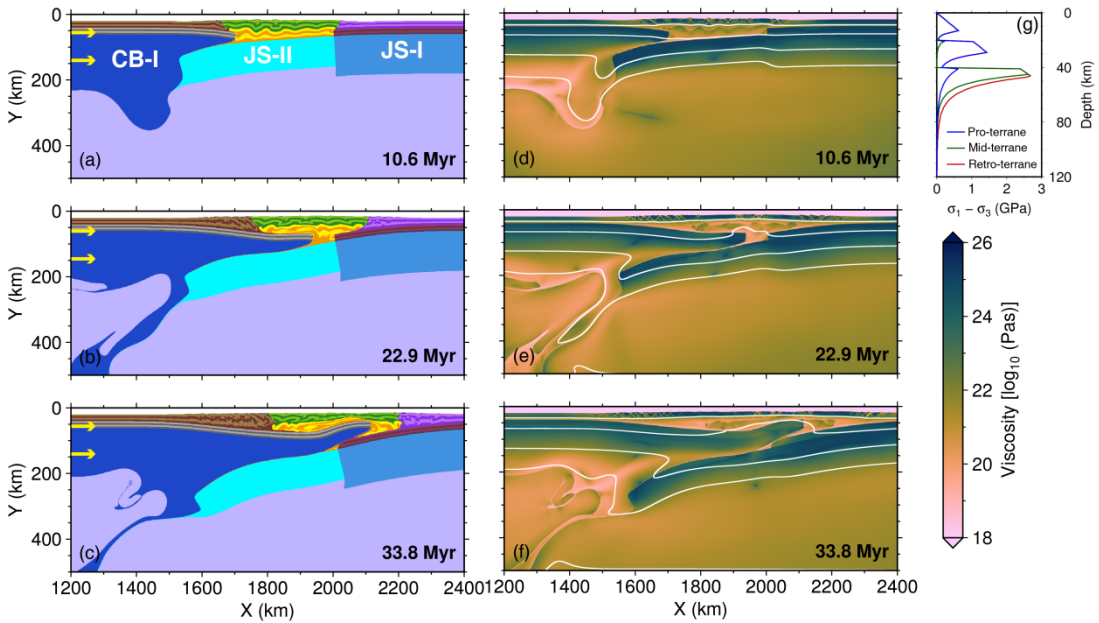
**Figure 6. Replacement of the lithosphere of the Pro-terrane.** Rheological models for the Pro-, Mid- and

736

737
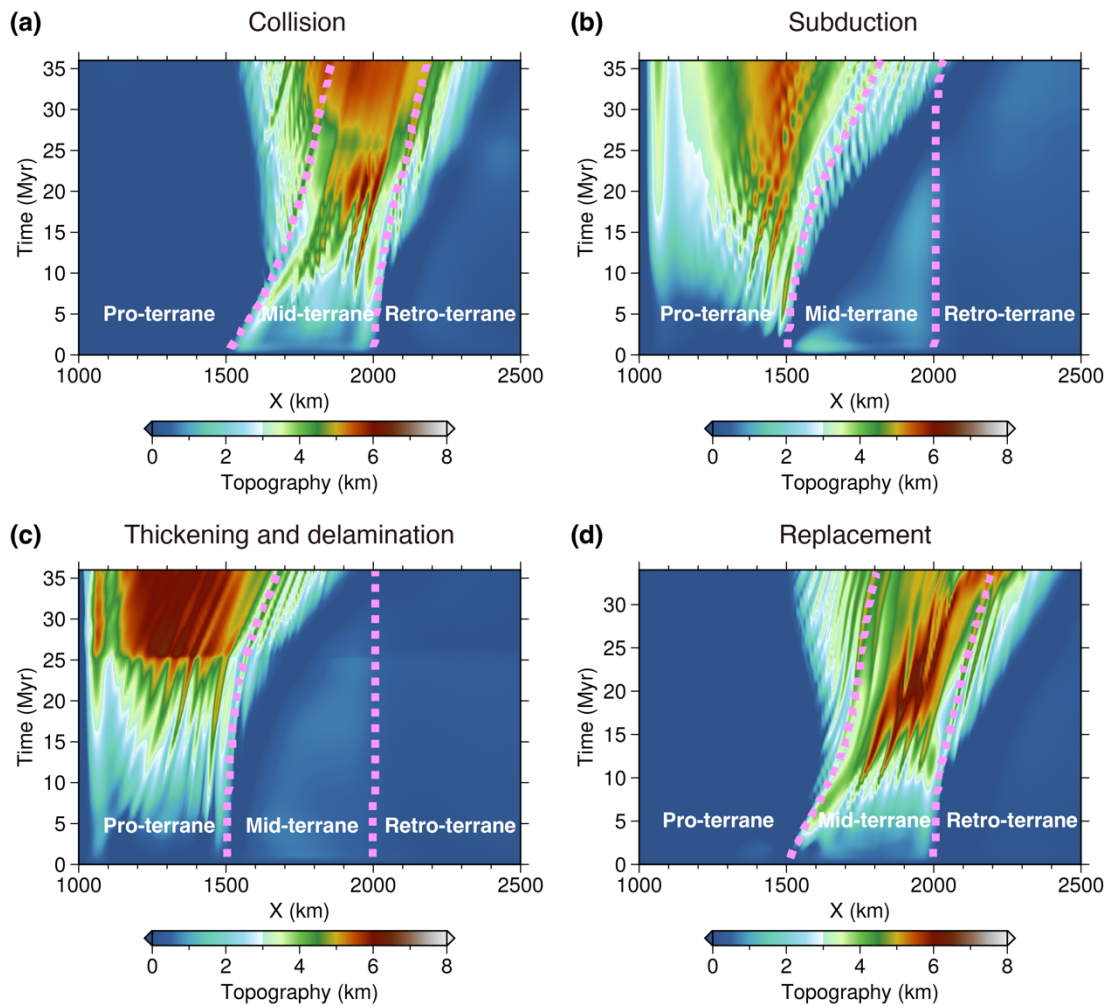
**Figure 7. Evolution of surface relief for the different deformation styles.** The purple dashed lines indicate the boundaries between terranes. (a) – (d) Surface relief associated with the deformation patterns of lithosphere collision, subduction, thickening and delamination, and replacement, respectively.

741

742
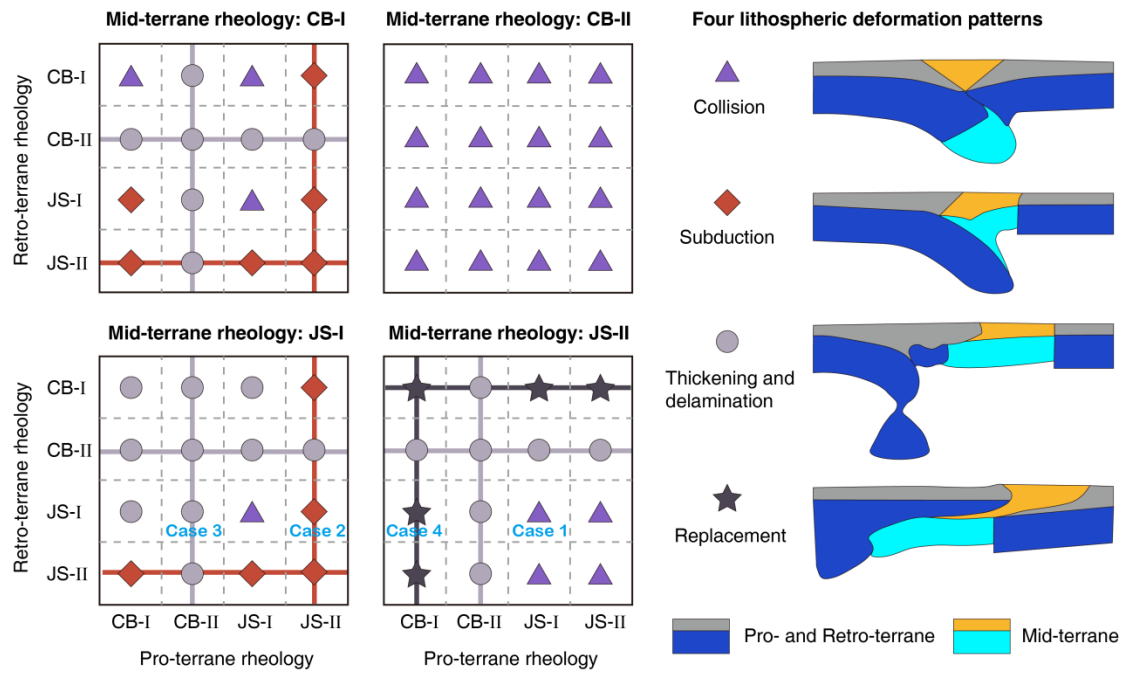
**Figure 8. Four styles of lithosphere deformation patterns.** Symbols with colors indicate different deformation

patterns of the lithosphere. Cases 1 – 4 are the selected models chosen to illustrate details of these modes of

compressional evolution.

746

747
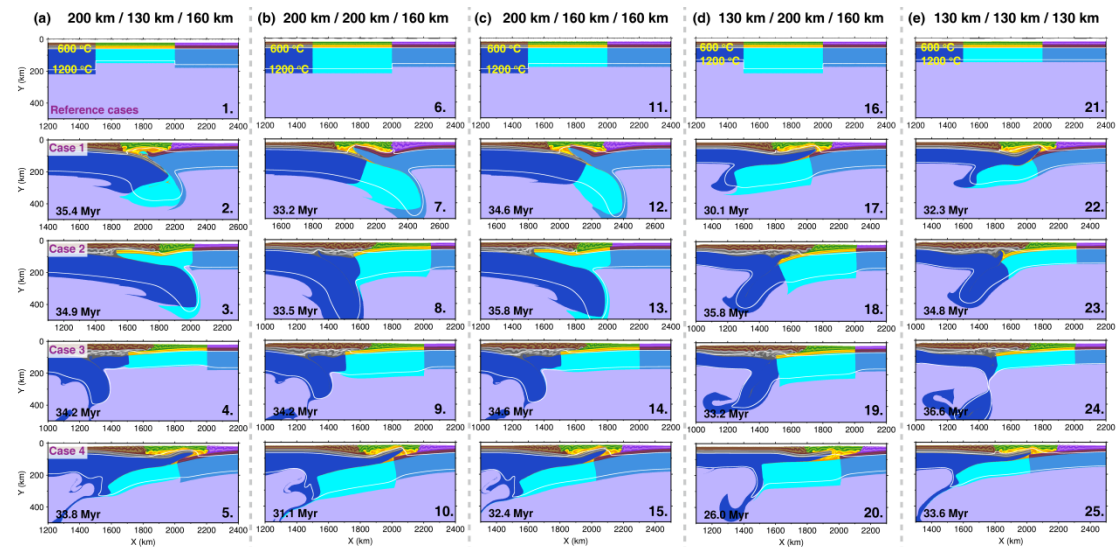
**Figure 9. Effects of lithosphere thicknesses of various terranes.** (a) – (e) Final simulation results of models with

the different lithosphere thicknesses of the Pro-, Mid-, and Retro-terranes, respectively. (a) Final simulation

results of reference cases. Rheological models of the Pro-, Mid- and Retro-terranes in 2 – 4 rows are same with

those in Cases 1 – 4, respectively.

752
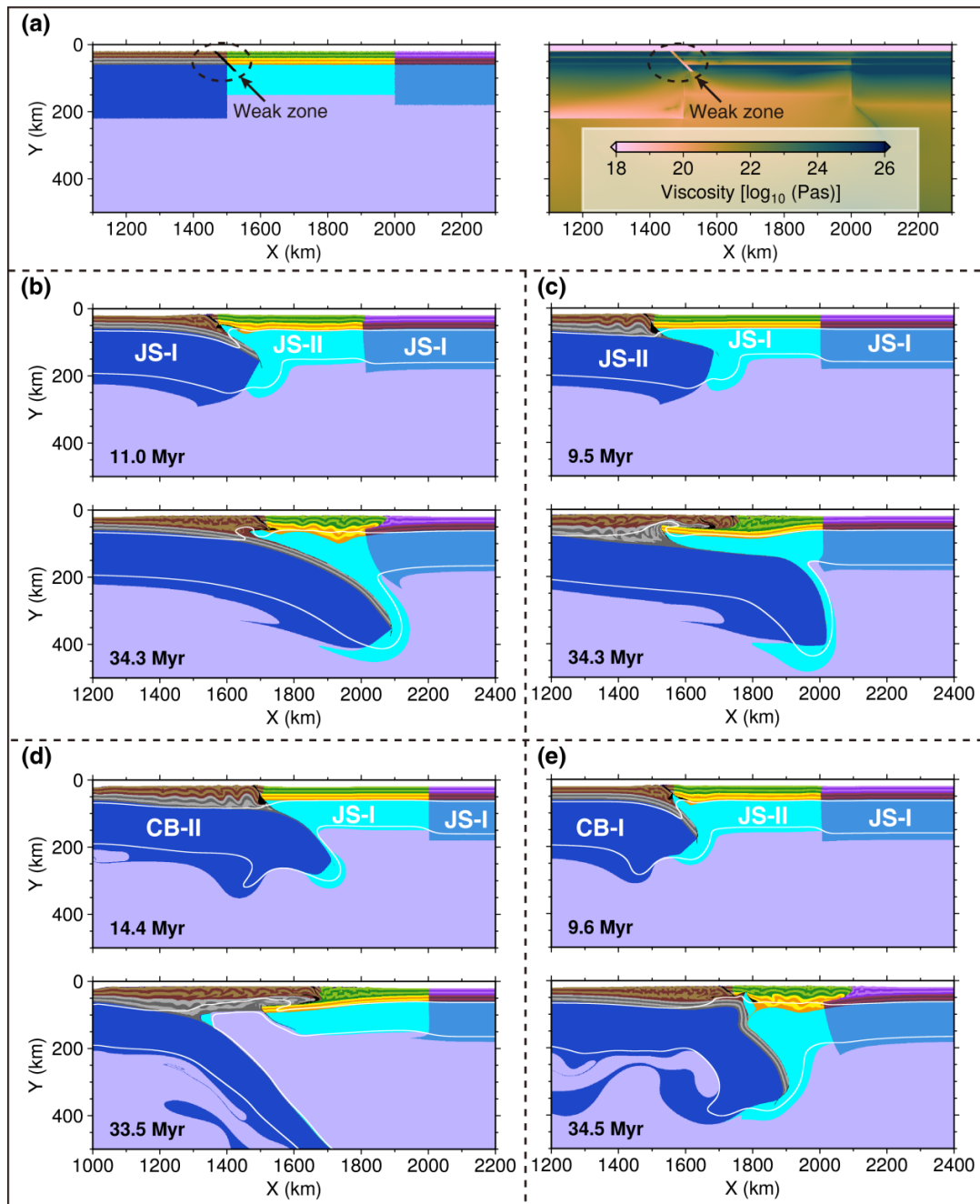
**Figure 10. Effects of local weak zone on lithosphere deformation.** (a) Details about the weak zone. (b) – (e) Final simulation results of models corresponding to Cases 1 – 4, respectively.

757
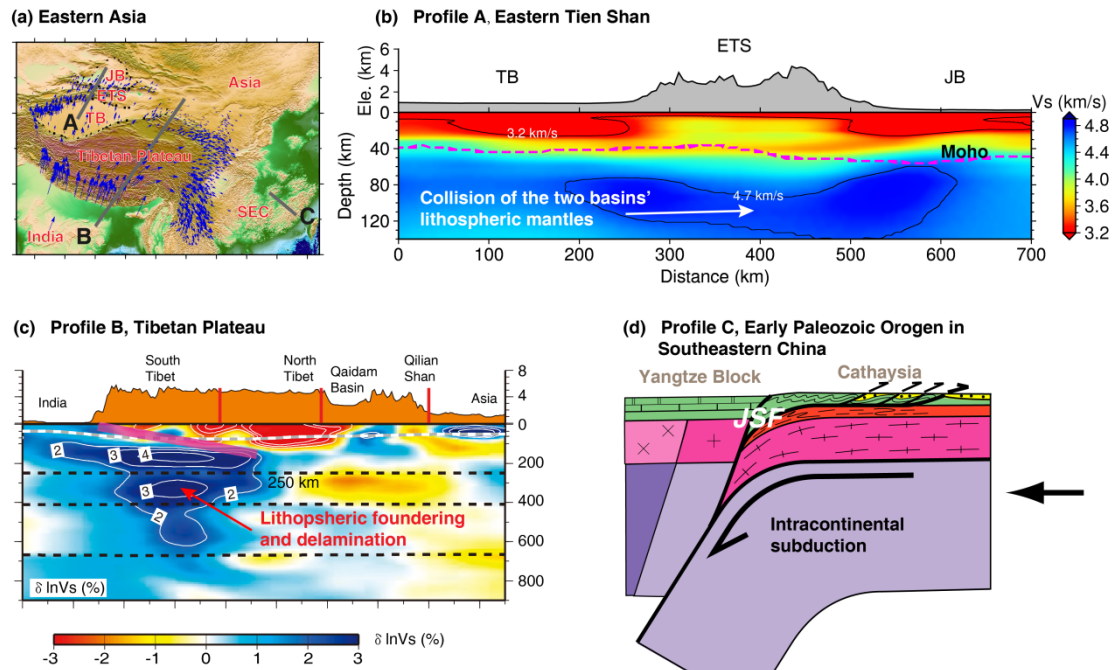
**Figure 11. Implications of simulation results to East Asia.** (a) Topography of East Asia. The three gray lines point out the locations of lithosphere profiles in (b), (c) and (d). TB, Tarim Basin; ETS, eastern Tien Shan; JB, Junggar Basin; SEC, Southeastern China. (b) Collision of the lithospheric mantle of Tarim Basin and Junggar Basin beneath the eastern Tien Shan (modified from Lü et al., 2019). (c) Lithospheric founding and delamination in the Tibetan Plateau (modified from Chen et al., 2017). (d) Intracontinental subduction in the Early Paleozoic Orogen in southeastern China (modified from Faure et al., 2009). JSF, Jiangshan–Shaoxing Fault.

764 **Table 1. Flow laws and material properties for different lithospheric layers.** $\rho_0$ is the initial density; it evolves

765 with time as $\rho = \rho_0 \left(1 - \alpha \left(T - T_0\right)\right)\left(1 + \beta \left(P - P_0\right)\right)$, where $T_0 = 20°$ C, $P_0 = 10^5$ MPa. Flow law: qtz. = quartzite, Plag.

766 = plagioclase, ol. = olivine.

| Material properties | Sediment | Upper crust | Lower crust | Lithospheric mantle | Asthenosphere |
|---|---|---|---|---|---|
| $\rho_0$ (kg/m³) | 2600 | 2700 | 2800 | 3300 | 3300 |
| Flow laws | Wet qtz. | Wet qtz. | Plag. | Dry ol. | Dry ol. |
| $1/A_D$ (Pa$^n$ s) | $1.97 \times 10^{17}$ | $1.97 \times 10^{17}$ | $4.80 \times 10^{22}$ | $3.98 \times 10^{16}$ | $3.98 \times 10^{16}$ |
| $n$ | 2.3 | 2.3 | 3.2 | 3.5 | 3.5 |
| $E_a$ (KJ/mol) | 154 | 154 | 238 | 532 | 532 |
| $V_a$ (J/bar) | 0.8 | 0.8 | 1.2 | 1.2 | 1.2 |
| $\phi = sin(\varphi)$ | 0.2 – 0.1 | 0.3 – 0.1 | 0.3 – 0.1 | 0.6 – 0.4 | 0.6 – 0.3 |
| $C$ (Pa) | $1 \times 10^{7\text{-}6}$ | $1 \times 10^{7\text{-}6}$ | $1 \times 10^{7\text{-}6}$ | $1 \times 10^{7\text{-}6}$ | $1 \times 10^{7\text{-}6}$ |
| $H_r$ (uW/m³) | 2.0 | 1.5 | 0.5 | 0.022 | 0.022 |
| $C_p$ (J/kg K) | 1000 | 1000 | 1000 | 1000 | 1000 |
| $\alpha$ (1/K) | $3 \times 10^{-5}$ | $3 \times 10^{-5}$ | $3 \times 10^{-5}$ | $3 \times 10^{-5}$ | $3 \times 10^{-5}$ |
| $\beta$ (1/MPa) | $1 \times 10^{-5}$ | $1 \times 10^{-5}$ | $1 \times 10^{-5}$ | $1 \times 10^{-5}$ | $1 \times 10^{-5}$ |
| $k$ (W/m/K) | 0.64+807/($T$+77) | 0.64+807/($T$+77) | 1.18+474/($T$+77) | [0.73+1293/($T$+77)] ×(1+0.00004$P$) | [0.73+1293/($T$+77)]× (1+0.00004) |

767